Thermodynamic Properties of Sr-Sn Alloys via Emf Measurements and Thermal Analysis

Nathan D. Smith[1,z], Jorge Paz Soldan-Palma[1], Yuran Kong[1], Zi-Kui Liu[1], Hojong Kim[1]

[1]Materials Science and Engineering, The Pennsylvania State University, 406 Steidle Building, University Park, PA 16802, United States of America

Author E-mail addresses: nsmith1453@gmail.com, jfp21@psu.edu, yxk42@psu.edu, liu@matse.psu.edu, huk29@psu.edu

Corresponding Author: Nathan D. Smith
[z]E-mail: nsmith1453@gmail.com. Tel: 301-639-9870

KEYWORDS: Sr-Sn alloys; emf measurements; thermodynamic properties

ABSTRACT

The thermochemical properties of Sr-Sn alloys were determined by electromotive force (emf) measurements to evaluate liquid tin as an interacting electrode material for separating alkaline-earth elements from molten salt solutions. A Sr(s)|CaF_2-SrF_2|Sr(in Sn) cell was used to measure emf values for twelve Sr-Sn alloys at mole fractions x_{Sr} = 0.02–0.43, allowing the determination of thermochemical properties such as activity and partial molar quantities of Gibbs energy, entropy, and enthalpy of Sr at 730–1110 K. Activity values of Sr in liquid Sn were as low as 6.9×10^{-12} at 800 K and x_{Sr} = 0.02 indicating highly non-ideal solution behavior between Sr and Sn. Phase transitions were also determined from the emf data and were validated via differential scanning calorimetry (DSC). Through the combination of emf measurements for thermochemical properties, X-ray diffraction (XRD) for phase constituents, and DSC measurements for phase transitions, this work established more complete thermodynamic properties of the Sr-Sn binary system.

INTRODUCTION

Strong atomic interactions resulting from the pairing of electropositive alkaline-earths and electronegative liquid metals (e.g., Bi and Sn) offer a unique approach for the recovery of Sr^{2+} ions from molten chloride solutions[1]. For instance, Li^+ ions are electrochemically active in ternary LiCl-KCl-$SrCl_2$ solution, implying that Sr^{2+} ions are not electrochemically separable from the solution. However, Sr^{2+} ions in LiCl-KCl-$SrCl_2$ solution were found to be electrodeposited into a liquid Bi cathode at 773 K[2], which was rationalized based upon the extremely low activity of Sr in liquid Bi (i.e., $a_{Sr} = 8.1\times10^{-14}$ at 773 K and $x_{Sr} = 0.05$)[3]. This result demonstrates that the most stable alkaline-earth ions in molten salts can be electrochemically separated using strongly-interacting low-melting liquid metals (T_m = 545 K for Bi and 505 K for Sn). The liquid metal electrodes may then allow for the recovery of alkaline-earth fission products (Sr and Ba) from the process salt (LiCl-KCl eutectic) utilized in electrorefining of used nuclear fuels for recycling uranium metal[4], and thus permit the reuse of the salts for minimizing secondary generation of nuclear waste.

In order to assess the viability of a liquid Sn electrode for the recovery of Sr from molten salts, this work investigated the thermochemical properties of Sr-Sn alloys over a wide range of Sr mole fractions (x_{Sr} = 0.02–0.43) and temperatures (730–1110 K) via electromotive force (emf) measurements in complement with thermal and structural analyses of the alloys.

The phase behavior of the Sr-Sn system has been investigated by a number of researchers, identifying six intermetallic compounds ($SrSn_4$, $SrSn_3$, Sr_3Sn_5, SrSn, Sr_5Sn_3, and Sr_2Sn) and phase transition temperatures by X-ray diffraction (XRD), microscopy, and thermal analysis[5–9]. Separately, Zhao et al. and Zhou et al. both compiled these experimental results and conducted thermodynamic assessments of the Sr-Sn system aided by first-principles calculations based on density functional theory (DFT)[10,11]. In addition, the activity values of Sr in Sn were measured via

emf measurements in KCl-$SrCl_2$ electrolytes by Volkovich et al. for dilute compositions (x_{Sr} = 0.001–0.03) at 973–1073 K[12] and by Klebanov et al. for x_{Sr} = 0.01–0.16 at 900 K using the coulometric titration technique[13]. However, accurate compositional accounting of Sr in liquid Sn via coulometric titration is challenging due to the high solubility of Sr metal in molten halide salts which can result in side reactions in an electrochemical cell and increased electronic conductivity of the electrolyte. For example, about 5.5–25 mol% Sr metal was reported to be soluble in molten $SrCl_2$ at 1112–1273 K[14]. In order to obtain reliable emf measurements over comprehensive compositions and temperatures, this work employed Sr-Sn alloys at fixed mole fractions and a solid-state CaF_2-SrF_2 electrolyte thereby eliminating concern for Sr metal dissolution into molten chlorides as well as the need for coulometric titration.

In this work, the electrochemical cell for emf measurements of Sr-Sn alloys was as follows:

$\underline{\text{Sr(s)}}$ | CaF_2-SrF_2 | Sr(in Sn), (1)

where the underlined pure Sr(s) acts as the reference electrode (RE), solid CaF_2-SrF_2 (97-3 mol%) as the electrolyte, and Sr-Sn alloy as the working electrode (WE). The half reactions in this electrochemical cell are:

WE: $Sr^{2+} + 2e^- = Sr(\text{in Sn})$ (2)

RE: $Sr^{2+} + 2e^- = Sr(s)$, (3)

and the overall cell reaction is:

$Sr(s) = Sr(\text{in Sn})$ (4)

For this cell reaction, the change in partial molar Gibbs energy (chemical potential) of Sr, $\Delta\bar{G}_{Sr}$, is given by:

$$\Delta\bar{G}_{Sr} = \bar{G}_{Sr(\text{in Sn})} - G^0_{Sr(s)} = RT\ln(a_{Sr(\text{in Sn})}), \quad (5)$$

where $\bar{G}_{\mathrm{Sr(in\ Sn)}}$ is the chemical potential of Sr in Sn, $G^0_{\mathrm{Sr(s)}}$ is the standard chemical potential of pure Sr, R is the universal gas constant, and T is the temperature in Kelvin. Then, the measured cell emf, E_{cell}, is directly related to the change in partial molar Gibbs energy of Sr and thus, the activity by the Nernst equation:

$$E_{\mathrm{cell}} = -\frac{\Delta\bar{G}_{\mathrm{Sr}}}{2F} = -\frac{RT}{2F}\ln\left(a_{\mathrm{Sr(in\ Sn)}}\right), \tag{6}$$

where F is the Faraday constant.

In order to achieve reliable and reproducible emf measurements, a less-reactive Sr-Bi alloy (x_{Sr} = 0.10) was used as the RE for emf measurements of Sr-Sn alloys instead of pure Sr whose reactivity resulted in an early failure of the electrochemical cell operation at elevated temperatures. Using the Sr-Bi as the RE, this electrochemical cell (I) and the cell potential (E_{I}) are:

I: Sr-Bi (x_{Sr} = 0.10) | CaF_2-SrF_2 | Sr(in Sn), $\qquad E_{\mathrm{I}} = -\frac{RT}{2F}\ln\left(\frac{a_{\mathrm{Sr(in\ Sn)}}}{a^*_{\mathrm{Sr(in\ Bi)}}}\right)$ (7)

where $a^*_{\mathrm{Sr(in\ Bi)}}$ is the activity of Sr in Bi at x_{Sr} = 0.10. The cell potential of this Sr-Bi alloy (E_{II}) was previously determined[3] relative to pure Sr(s) at 754–1009 K using the following electrochemical cell (II):

II: Sr(s) | CaF_2-SrF_2 | Sr-Bi (x_{Sr} = 0.10), $\qquad E_{\mathrm{II}} = -\frac{RT}{2F}\ln\left(a^*_{\mathrm{Sr(in\ Bi)}}\right)$ (8)

and exhibited a linear variation as a function of temperature according to:

$E_{\mathrm{II}} = 6.9\times10^{-5}\ T + 0.922$ [V]. (9)

The emf values of Sr-Sn alloys (E_{cell}) relative to pure Sr(s) can be determined by adding these two cell potentials:

$$E_{\mathrm{cell}} = E_{\mathrm{I}} + E_{\mathrm{II}} = -\frac{RT}{2F}\ln\left(a_{\mathrm{Sr(in\ Sn)}}\right). \tag{10}$$

Moving forward in the manuscript, $a_{\mathrm{Sr(in\ Sn)}}$ will be denoted by a_{Sr} for simplicity.

EXPERIMENTAL

Electrochemical cell components and assembly

The solid CaF_2-SrF_2 (97-3 mol%) electrolyte was prepared by ball-milling 350 g of high-purity CaF_2 (99.5%, Alfa Aesar, Stock No. 11055), 17.4 g of high-purity SrF_2 (99.99%, Sigma-Aldrich, Stock No. 450030), and 25 g of polyvinyl alcohol binder (Sigma-Aldrich, Stock No. 341584) in isopropanol for 24 h. The mixture was dried in air for 24 h and approximately 130 g of powder was taken and uniaxially pressed at 30 MPa into a pellet (75 mm diameter × 17 mm thickness). Seven wells (each with 11.2 mm diameter × 12 mm depth) were drilled into the pellet with one well in the center and six wells evenly spaced 25.4 mm away from the center (Figure 1). Similarly, electrolyte caps (19 mm diameter × 10 mm height) were fabricated from 4 g of the mixture with a 1.1 mm hole drilled through the center. These green pellets were fired in air at 393 K for 12 h to remove moisture, 823 K for 12 h to burn away the binder, and 1273 K for 3 h to sinter; the high temperature (823 K) and long dwell time (12 h) were selected to thoroughly burn away the PVA binder, leaving a negligible quantity of carbon residue.

Sr-Sn alloys at specific compositions were fabricated from Sn pieces (99.9999%, Alfa Aesar, Stock No. 45481) and Sr ingot (99%, Sigma-Aldrich, Stock No. 343730) using an arc melter (MAM-1, Edmund Bühler GmbH) under argon atmosphere. The Sr-Bi alloy (x_{Sr} = 0.10) for the RE was fabricated in the same manner from Sr ingot and Bi pieces (99.999%, Sigma-Aldrich, Stock No. 556130). Induction coupled plasma-optical emission spectroscopy (ICP-OES, Thermo iCAP 7400) was used to verify the compositions of the arc-melted Sr-Sn alloys with a maximum of 4 % error of the measured value. The alloy electrodes were machined into a cylindrical shape (10 mm diameter × 7 mm thickness) with a centering hole drilled partway through for the tungsten electrical lead.

Final assembly of the electrochemical cell was performed in a glovebox under an inert argon environment (O_2 < 0.5 ppm) to mitigate the rapid oxidation of the electrodes. The CaF_2-SrF_2 electrolyte was placed in an alumina crucible (8.2 cm diameter × 3.0 cm height). The tungsten wires (1 mm diameter × 46 cm length) were insulated with mullite tubes (0.64 cm outer diameter × 30.5 cm length) and inserted through the stainless-steel top flange, through the CaF_2-SrF_2 caps, and into the electrodes. The electrolyte caps were installed to minimize the cross-contamination of electrodes through vapor-phase transport during the measurements at elevated temperatures. The test chamber was then sealed, removed from the glovebox, loaded into a crucible furnace, and evacuated to ~1 Pa. The test chamber was heated at 373 K for 12 h, at 543 K for 12 h under vacuum to remove residual moisture and oxygen, purged three times with high purity argon, and finally heated to 1023 K under flowing argon (~10 mL min^{-1}) to melt the electrodes for establishment of electrical contact between each electrode, the tungsten wire, and the electrolyte. The cell temperature was measured using a thermocouple (ASTM type-K) located at the center of the electrolyte, and a thermocouple data acquisition system (NI 9211, National Instruments).

Emf measurements

Emf measurements were performed by measuring the potential difference between the RE (Sr-Bi, x_{Sr} = 0.10) and each WE sequentially in 180 s intervals during thermal cycles using a potentiostat-galvanostat (Autolab PGSTAT302N, Metrohm AG). Emf data were collected throughout a cooling and reheating cycle between 1123 K and 723 K in 25 K increments. The cell temperature was held constant at each increment for 1.5 h to reach thermal and electrochemical equilibria and ramped at ±5 K min^{-1} between increments. In each increment, the last data approached a steady state thermally (dT/dt < 0.05 K s^{-1}) and electrochemically (dE/dt < 0.01 mV s^{-1}), and these data were considered for thermodynamic analyses.

Structural and thermal analyses of Sr-Sn alloys

Crystal structures of the Sr-Sn alloys were characterized using an X-ray diffractometer (XRD, PANalytical Empyrean). Sr-Sn alloys were annealed at ~15 K below their solidus temperatures for 24 h to determine near-equilibrium phases. The annealed alloys were ground into a fine powder using a mortar and pestle in an Ar-filled glovebox and then coated with mineral oil to minimize oxidation during the XRD measurements. A broad amorphous background from mineral oil at low angles ($10\ ° < 2\theta < 20\ °$) was subtracted to facilitate the identification of crystalline phase peaks of the Sr-Sn alloys.

Differential scanning calorimetry (DSC) was performed using a thermal analyzer (Netzsch Instruments, STA 449 F3 Jupiter) to detect phase transition temperatures. Between 20–50 mg of each annealed alloy sample was placed in the alumina crucible with a thin, inert tungsten foil interlayer (4.8 mm diameter × 0.1 mm thickness) as a reaction barrier between the Sr-Sn alloy and alumina crucible. Thermal analyses were conducted at multiple scan rates of 5–20 K min^{-1}. In determining the liquidus temperature, the endpoint of the transition was utilized as the endpoint represents the termination of the liquidus transition during the heating cycle; endpoint values at varying scan rates were extrapolated to 0 K min^{-1}. For other transitions (e.g. eutectic, peritectic), the average of the onset temperatures from all scan rates was used[15]. The Sr-Sn alloys with $x_{Sr} > 0.30$ were found to react with the alumina crucible despite the tungsten interlayer; therefore, a small graphite cap (~5 mm diameter × 2 mm height) was placed over samples to protect the instrument.

RESULTS AND DISCUSSION

Emf measurements

Using the electrochemical cell described in Eq. (7), the cell potentials (E_I) of Sr-Sn alloys at x_{Sr} = 0.02–0.43 were measured relative to the Sr-Bi alloy (x_{Sr} = 0.10) at 730–1110 K. An exemplary plot of real-time cell potential and temperature is shown for x_{Sr} = 0.17 (Figure 2), indicating the reliable emf values with high stability at each temperature step ($dE_I/dt < 0.01$ mV s^{-1}) and reproducibility between cooling and heating cycles (< 5 mV difference). Using Eqs. (9) and (10), emf values (E_{cell}) of Sr-Sn alloys vs. pure Sr(s) were plotted as a function of temperature for twelve compositions at x_{Sr} = 0.02–0.43 (Figure 3). Emf data from both the heating and cooling cycles are presented up to x_{Sr} = 0.26 while the data from the cooling cycle are presented at x_{Sr} = 0.30–0.43 due to increased instability observed during the reheating cycle. The emf of Sr-Sn alloys decreased as Sr content (x_{Sr}) increased at a given temperature.

Mole fractions x_{Sr} = 0.02–0.08 remained in the liquid phase over the entirety of the measured temperature range and their emf values changed linearly as a function of temperature. Mole fractions x_{Sr} = 0.10–0.22 were subjected to the first-order liquidus transition (L = L + $SrSn_3$), indicated by the discontinuity in the slope (the first-order derivative, dE_{cell}/dT). The emf trajectories of x_{Sr} = 0.10–0.22 were nearly identical in the [L + $SrSn_3$] region due to invariant activity in a two-phase region in equilibrium (Gibbs phase rule). Similar equilibrium behavior was also observed in the two-phase [L + Sr_3Sn_5] region for x_{Sr} = 0.26–0.33 according to their identical emf trajectories. While similar emf trajectories are expected for x_{Sr} = 0.26–0.33 below the solidus temperature (~860 K) with two equilibrium phases of [$SrSn_3$ + Sr_3Sn_5], the measured emf trajectories were not agreeing each other and x_{Sr} = 0.26 followed the trajectory of x_{Sr} = 0.10–0.22 in two-phase [L + $SrSn_3$] region. Such non-equilibrium behavior implies the presence of metastable phases from non-equilibrium cooling (solidification) and was also noticeable for higher Sr mole fractions x_{Sr} = 0.39–0.43 whose equilibrium phases are [Sr_3Sn_5 + SrSn] below solidus

(~1078 K). For instance, the emf of x_{Sr} = 0.39 deviated from that of x_{Sr} = 0.43 and followed that of x_{Sr} = 0.33.

Overall, a reliable set of emf data was obtained when the alloys contain a liquid phase based on the low hysteresis in emf values between thermal cycles and the clear detection of first-order transition temperatures (Figure 3). Below solidus, non-equilibrium emf trajectory was observed possibly due to the formation of metastable phases from non-equilibrium cooling. The transition temperatures and phase constituents of the alloys were further investigated using XRD and DSC for selected compositions.

Structural and thermal characterization

The Sr-Sn alloys (x_{Sr} =0.04–0.43) were annealed at 15 K below solidus for 24 h and their phase constituents were characterized by comparing the measured XRD patterns to the reported diffraction patterns of Sr-Sn intermetallic compounds[16,17] (Figure 4), summarized in Table 1. All four reported intermetallic compounds ($SrSn_4$, $SrSn_3$, Sr_3Sn_5, and SrSn) were observed; however, the presence of non-equilibrium phases was apparent at x_{Sr} = 0.22–0.43 despite the 24 h of annealing (Table 1). For example, the $SrSn_4$ phase was observed at x_{Sr} = 0.26 despite the expectation of only two equilibrium phases ($SrSn_3$ and Sr_3Sn_5) the $SrSn_3$ phase remains observable at x_{Sr} = 0.39–0.43 in addition to Sr_3Sn_5 and SrSn. The XRD measurements of annealed samples confirmed the presence of metastable phases from non-equilibrium solidification of Sr-Sn alloys, supporting the non-equilibrium emf trajectories for x_{Sr} = 0.26–0.39 (Figure 3).

The first-order transition temperatures of Sr-Sn alloys (x_{Sr} = 0.02–0.43) were determined from DSC measurements during the heating cycle (450–1350 K) and exemplary DSC results at 5 K min^{-1} are presented in Figure 5. The DSC results clearly indicate four characteristic (I–IV) and liquidus transitions which are summarized in Table 2 at each mole fraction, compared to transitions

estimated from emf measurements. The four characteristic transitions from this work are listed in Table 3 and compared to the previous works in the literature[6,7,9].

The liquidus transition temperatures from DSC were in excellent agreement with those estimated from emf measurements with less than a 10 K difference (Table 2). The eutectic transition [I: L = Sn + $SrSn_4$] was observed at 496 K in excellent agreement with other reported values within 9 K. Three peritectic transitions from DSC measurements were at 618 K for [II: L + $SrSn_3$ = $SrSn_4$]; 860 K for [III: L + Sr_3Sn_5 = $SrSn_3$] in excellent agreement with emf results at 860 K; and 1079 K for [IV: L + SrSn = Sr_3Sn_5] in agreement with emf results at 1079 K.

However, the peritectic transitions (II–IV) were significantly different among the reported values: about 11 K difference from Marshall and Chang[7], 27–30 K from Palenzona and Pani[9], and 7–15 K from Widera and Schäfer[6] (Table 3). The discrepancy in thermal analysis is thought to come from the variety in crucible materials (W, Mo, graphite, Al_2O_3, and SiO_2) selected for containing Sr-Sn alloys (Table 3). From the standpoint of materials compatibility, the oxide crucibles used by Widera and Schäfer[6] might react with Sr in liquid Sr-Sn due to high oxygen affinity of Sr, and the Mo crucible by Palenzona and Pani[9] can react with liquid Sn to form intermetallic compounds ($MoSn_2$ and MoSn)[18], both resulting in side reactions during thermal analyses. The use of inert W foil is thought to result in more reliable DSC measurements, which agree well with the results from emf measurements as well as with the results from Marshall and Chang who employed inert graphite crucibles for their thermal analysis[7].

The transition temperatures in this work are overlaid onto the recent Sr-Sn phase diagram assessed by Zhao et al. using the CALPHAD method[10]. The liquidus transitions agree well with the assessed phase diagram with discrepancies found for the three peritectic transitions (II–V) as

Zhao et al. utilized the results from Palenzona and Pani for thermodynamic assessment of Sr-Sn system[9,10].

Thermochemical properties of the Sr-Sn system

The emf data (E_{cell} vs. T) was used to calculate thermochemical properties, including the activity and the changes in partial molar entropy ($\Delta\bar{S}_{\text{Sr}}$) and enthalpy ($\Delta\bar{H}_{\text{Sr}}$) using the Nernst and Gibbs-Helmholtz relations:

$$E_{\text{cell}} = -\frac{\Delta\bar{G}_{\text{Sr}}}{2F} = -\frac{\Delta\bar{H}_{\text{Sr}}}{2F} + T\frac{\Delta\bar{S}_{\text{Sr}}}{2F} \quad (11)$$

$$\Delta\bar{S}_{\text{Sr}} = -\left(\frac{\partial\Delta\bar{G}_{\text{Sr}}}{\partial T}\right)_P = 2F\left(\frac{\partial E_{\text{cell}}}{\partial T}\right)_P \quad (12)$$

$$\Delta\bar{H}_{\text{Sr}} = -T^2\left(\frac{\partial\Delta\bar{G}_{\text{Sr}}/T}{\partial T}\right)_P = -2F\left(\frac{\partial(E_{\text{cell}}/T)}{\partial(1/T)}\right)_P \quad (13)$$

When E_{cell} vs. T is linear (denoted by solid lines in Figure 3), $\Delta\bar{S}_{\text{Sr}}$ and $\Delta\bar{H}_{\text{Sr}}$ are temperature-independent and can be estimated from the slope and the intercept at 0 K, respectively. For curved, non-linear behavior in E_{cell} vs. T (denoted by dashed lines in Figure 3), the data in the two-phase region were fit to the following general fitting equation:

$$E_{\text{cell}} = A + BT + CT\ln(T), \quad (14)$$

where A, B, and C are fitting parameters. The linear fits and related partial molar quantities are reported in Table 4 and the curved fit parameters are reported in Table 5.

Using the linear or non-linear fit of each alloy, the thermochemical properties of Sr in Sn were calculated at 800 K, 900 K, and 1000 K, including emf, activity, and the partial molar excess Gibbs energy ($\bar{G}^{\text{E}}_{\text{Sr}}$) according to:

$$\bar{G}^{\text{E}}_{\text{Sr}} = RT(\ln a_{\text{Sr}} - \ln x_{\text{Sr}}). \quad (15)$$

The resulting values are listed below (Table 6) and are depicted graphically for T = 900 K (Figure 7).

Emf decreases as a function of x_{Sr} in the liquid phase and remains constant in the two-phase [L + Sr_3Sn_5] region due to invariant activity independent of a change in mole fraction, demonstrating equilibrium behavior of Sr-Sn alloys up to x_{Sr} = 0.33 (Figure 7a). In addition, the activity of Sr in liquid Sn is as low as $a_{Sr} = 8.4\times10^{-11}$ at 900 K and x_{Sr} = 0.02 (Figure 7b), indicating strong atomic interactions with a large excess Gibbs energy value of $\bar{G}_{Sr}^{E}$ = –144 kJ mol^{-1} (Figure 7c). Based upon the emf values of various liquid metals at 900 K near x_{Sr} = 0.10, the chemical interaction of liquid Sn (E_{cell} = 0.776 V) with Sr is thought to be stronger than Pb (E_{cell} = 0.725 V)[19], but weaker than Bi (E_{cell} = 0.981 V)[3] or Sb (E_{cell} = 1.111 V)[20].

The emf data in this work shows a similar trend with the results from Klebanov et al. who investigated the Sr-Sn alloys up to x_{Sr} = 0.16 by depositing Sr into liquid Sn via coulometric titration in molten KCl-$SrCl_2$ (55-45 mol%) electrolyte at 900 K[13]. The emf values from Klebanov et al. were consistently greater than this work by about 54–84 mV at similar mole fractions (Figure 7a). Similarly, Volkovich et al. determined emf values of dilute Sr compositions in molten KCl-$SrCl_2$ (74-26 mol%) electrolyte at 973–1073 K via coulometric titration[12]. At 973 K, the emf of x_{Sr} = 0.02 was estimated at 0.994 V vs. pure Sr(s), compared to this work at 0.909 V (Table 4). The discrepancy from prior works based on coulometric titration in KCl-$SrCl_2$ is thought to originate from uncertainties in compositional accounting (coulombic loss) of reactive Sr into liquid Sn. Considering reproducible emf results in this work at 730–1110 K during thermal cycles and their compliance with DSC measurements for verified mole fractions by ICP-OES, the emf data in this work is deemed to be more reliable.

Thermodynamic properties of the binary Sr-Sn system assessed by Zhao et al.[10] and Zhou et al.[11] were compared to the experimental results at 900 K (Figure 7). The assessed properties by Zhao et al. agree well with the experimental results from Klebanov et al. while the properties by Zhou et al. agree better with this work. In addition, the liquidus composition from Zhou et al. properly describe invariant activity in two-phase [L + Sr_3Sn_5] region at 900 K. It is noted that the discrepancy between two independent CALPHAD approaches implies the importance of reliable experimental data in thermodynamic assessment of alloys, in particular for strongly interacting liquid solutions.

CONCLUSIONS

Thermodynamic properties of the binary Sr-Sn system were determined via emf measurements over a wide range of mole fractions up to x_{Sr} = 0.43 at 730–1110 K, including activities, partial molar entropies, enthalpies, and excess Gibbs energies. The emf results with solid CaF_2-SrF_2 electrolyte were reproducible between thermal cycles and internally consistent among various mole fractions. Furthermore, the phase transitions detected during emf measurements were in excellent agreement with the DSC measurements, indicating reliable thermodynamic property measurements in this work.

From this experimental work, the activity of Sr in Sn was found to be as low as 6.9×10^{-12} at 800 K and x_{Sr} = 0.02, indicating strong interactions between Sr and Sn. These strong interactions coupled with a high solubility of Sr in liquid Sn (~18 mol% at 800 K) and low melting temperature (T_m = 505 K) suggest the utility of Sn or Sn-based alloys as electrode materials for recovery of alkaline-earth elements from molten salts.

Conflicts of Interest

There are no conflicts to declare.

Author Contributions

The manuscript was written through contributions of all authors. All authors have given approval to the final version of the manuscript.

Funding Sources

US Department of Energy, Office of Nuclear Energy

US National Science Foundation

Acknowledgements

This work was supported by the US National Science Foundation (grant number: CMMI-1662817) and the US Department of Energy, Office of Nuclear Energy's Nuclear Energy University Programs (Award No. DE-NE0008757).

References

1. H. Kim, N. Smith, K. Kumar, and T. Lichtenstein, *Electrochim. Acta*, **220**, 237–244 (2016).

2. T. Lichtenstein, T. P. Nigl, N. D. Smith, and H. Kim, *Electrochim. Acta*, **281**, 810–815 (2018).

3. N. D. Smith, T. Lichtenstein, J. Gesualdi, K. Kumar, and H. Kim, *Electrochim. Acta*, **225**, 584–591 (2017).

4. M. F. Simpson, *Sci. Technol. Nucl. Install.*, **945858** (2013).

5. K. W. Ray, *Ind. Eng. Chem.*, **22**, 519–522 (1930).

6. A. Widera and H. Schafer, *J. Less-Common Met.*, **77**, 29–36 (1981).

7. D. Marshall and Y. A. Chang, *J. Less-Common Met.*, **78**, 139–145 (1981).

8. F. Zurcher, R. Nesper, S. Hoffmann, and T. F. Fassler, *Z. Anorg. Allg. Chem*, **627**, 2211–2219 (2001).

9. A. Palenzona and M. Pani, *J. Alloys Compd.*, **384**, 227–230 (2004).

10. J. Zhao, Y. Du, L. Zhang, A. Wang, L. Zhou, D. Zhao, and J. Liang, *Thermochim. Acta*, **529**, 74–79 (2012).

11. B. Zhou, S. Shang, and Z. Liu, *Calphad*, **46**, 237–248 (2014).

12. A. V. Volkovich, V. I. Zhuravlev, and I. S. Trofimov, *Russ. Metall.*, 149–154 (2012).

13. E. B. Klebanov, O.O. Tvaradze, and A. G. Morachevskii, *Izv. Vyss. Uchebn. Zaved., Tsvetn. Met.*, **5**, 106–107 (1985).

14. H. Kim, D. Boysen, J. Newhouse, B. Spatocco, B. Chung, P. Burke, D. Bradwell, K. Jiang, A. Tomaszowska, K. Wang, W. Wei, L. Ortiz, S. Barriga, S. Poizeau, and D. Sadoway, *Chem. Rev.*, **113**, 2075–2099 (2013).

15. W. J. Boettinger, U. R. Kattner, K.-W. Moon, and J. H. Perepezko, *Methods Phase Diagr. Determ.*, 151–221 (2007).

16. G. Bergerhoff, R. Hundt, R. Sievers, and I. D. Brown, *Journal of Chemical Information and Computer Sciences*, **23**, 66-69 (1983).

17. R. T. Downs and M. Hall-Wallace, *American Mineralogist*, **88**, 247-250 (2003).

18. T. B. Massalski, L. Brewer, and R. H. Lamoreaux, *Binary Alloy Phase Diagrams*, 2nd ed., p. Vol 3., 2667-2669, (1990).

19. T. Nigl, T. Lichtenstein, N.D. Smith, J. Gesualdi, Y. Kong, and H. Kim, *Electrochim. Acta*, **165**, 991–998 (2018).

20. N. D. Smith, N. Orabona, T. Lichtenstein, J. Gesualdi, T. Nigl, and H. Kim, *Electrochim. Acta*, **305**, 547–554 (2019).

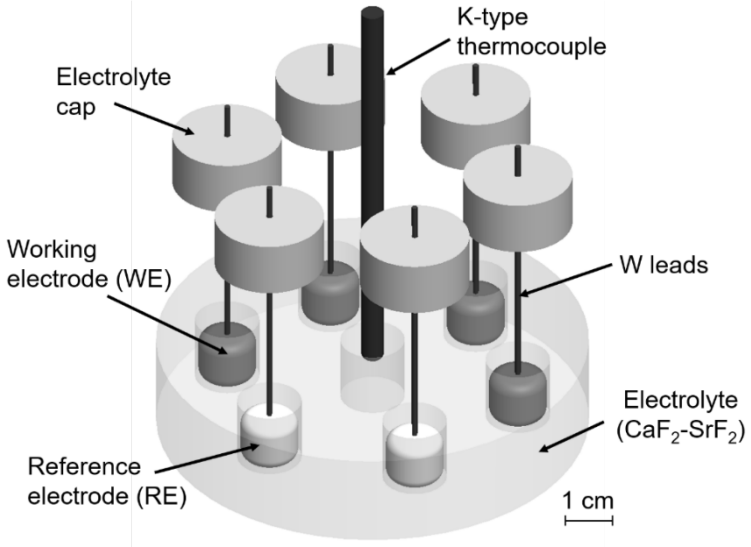

Figure 1. Schematic of the experimental set-up for emf measurements, comprised of four Sr-Sn WEs and two Sr-Bi REs at $x_{Sr(in\ Bi)} = 0.10$ in solid CaF_2-SrF_2 (97-3 mol%) electrolyte.

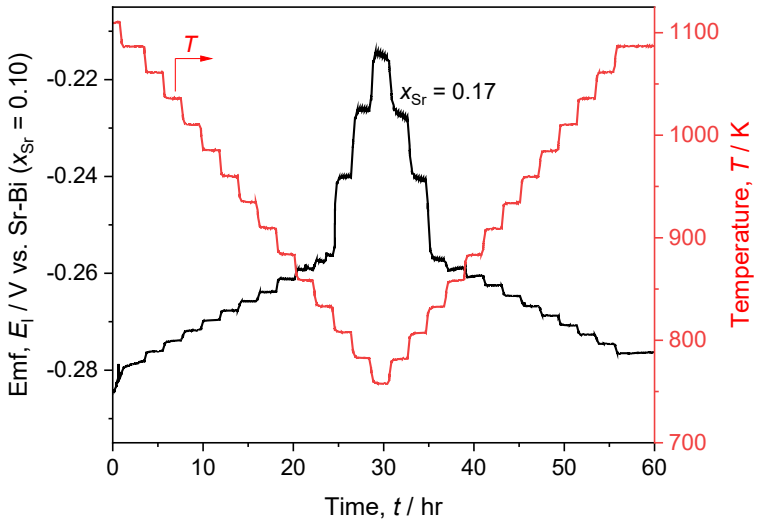

Figure 2. The cell potential (E_I) and temperature as a function of time upon cooling and heating a Sr-Bi ($x_{Sr} = 0.10$)|CaF_2-SrF_2|Sr-Sn ($x_{Sr} = 0.17$) cell.

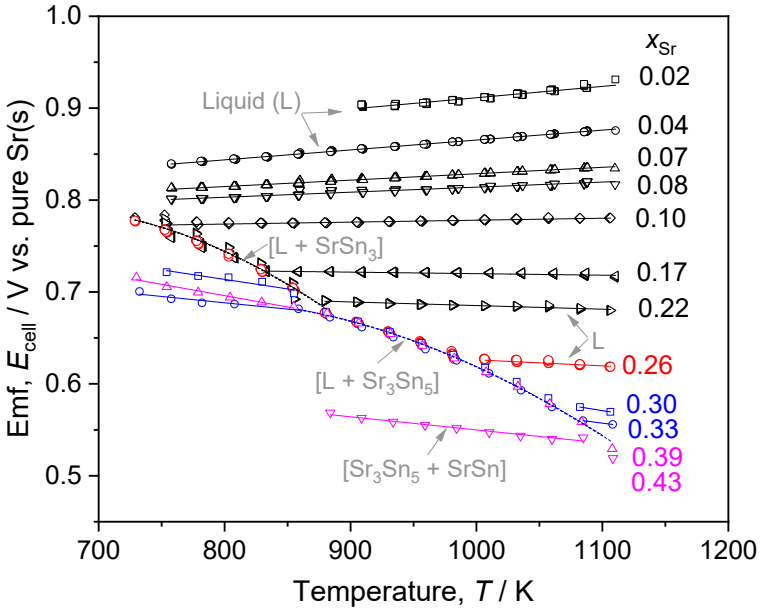

Figure 3. Emf values of Sr-Sn alloys, E_{cell} vs. pure Sr(s), as a function of temperature for x_{Sr} = 0.02–0.43.

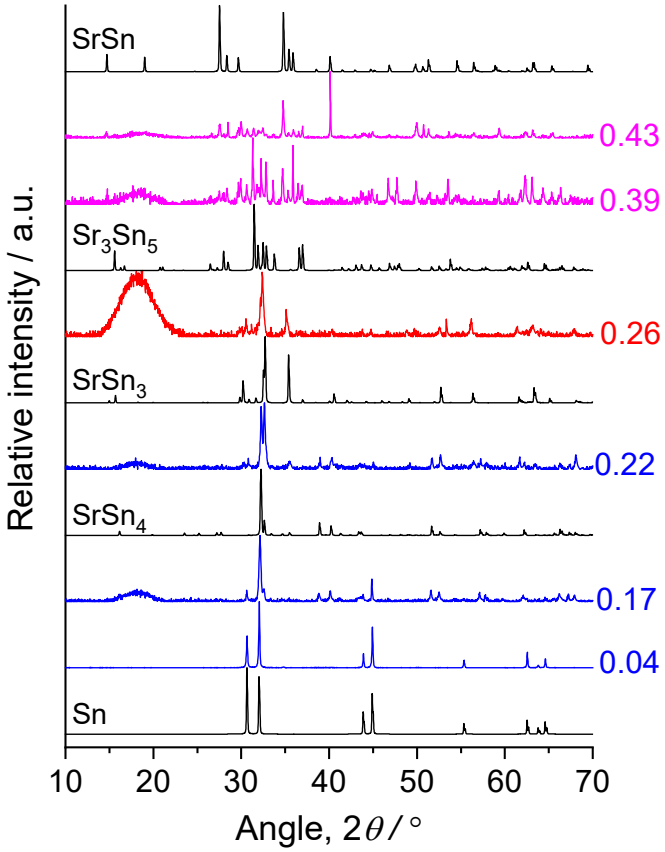

Figure 4. XRD patterns of Sr-Sn alloys (x_{Sr} = 0.04–0.43), compared to the reported diffraction patterns of Sr-Sn intermetallic compounds[16,17].

Table 1. Crystal structures identified in the Sr-Sn binary system by XRD patterns at each mole fraction, where the equilibrium phases are marked in bold.

x_{Sr}	Phases detected
0.04, 0.17	**Sn, $SrSn_4$**
0.22	Sn, **$SrSn_4$, $SrSn_3$**
0.26	$SrSn_4$, **$SrSn_3$, Sr_3Sn_5**
0.39, 0.43	$SrSn_3$, **Sr_3Sn_5, SrSn**

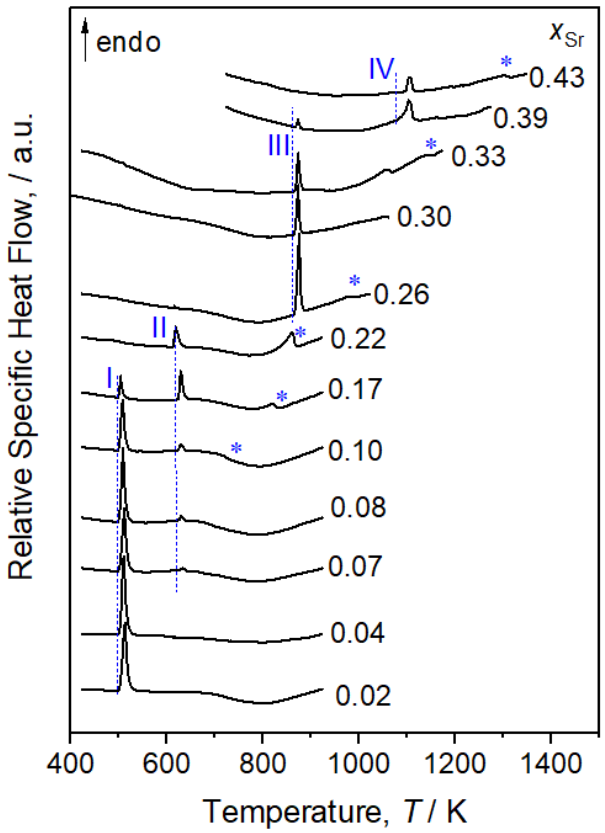

Figure 5. DSC scans of Sr-Sn alloys (x_{Sr} = 0.02–0.43) at 5 K min^{-1}, indicating four characteristic transition reactions (I–IV) and liquidus transitions (*).

Table 2. Summary of the transition temperatures (T_{trs}) from DSC measurements for phase transitions I–IV and liquidus.

	T_{trs} (K)				
x_{Sr}	I	II	III	IV	liquidus
0.02	497 (±2)	—	—	—	—
0.04	497 (±1)	—	—	—	—
0.07	496 (±1)	622 (±1)	—	—	—
0.08	495 (±1)	619 (±2)	—	—	—
0.10	496 (±1)	619 (±1)	—	—	735 (±3) / 744[a]
0.17	496 (±2)	619 (±2)	—	—	832 (±5) / 831[a]
0.22	—	610 (±3)	—	—	866 (±6) / 871[a]
0.26	—	—	859 (±7) / 868[a]	—	989 (±5) / 986[a]
0.30	—	—	856 (±9) / 858[a]	—	— / 1054[a]
0.33	—	—	863 (±3) / 859[a]	1079[a]	1155 (±8)
0.39	—	—	862 (±3) / 856[a]	1078 (±1)	—
0.43	—	—	—	1078 (±4)	1314 (±10)

[a]: transition temperatures were estimated from emf measurements (Figure 2) based on the discontinuity in the slope (dE_{cell}/dT).

Table 3. Four characteristic transitions (I–IV) from DSC measurements in Table 2, compared with previous experimental results by thermal analysis.

T_{trs} (K)	Reaction (type)	This work DSC / emf	Marshall & Chang [7]	Palenzona & Pani [9]	Widera & Schäfer [6]
I	$L = Sn + SrSn_4$ (eutectic)	496 (±2)	503 (±2)	503	505
II	$L + SrSn_3 = SrSn_4$ (peritectic)	618 (±8)	607 (±4)	588	611
III	$L + Sr_3Sn_5 = SrSn_3$ (peritectic)	860 (±4) / 860(±8)	871 (±1)	833	853
IV	$L + SrSn = Sr_3Sn_5$ (peritectic)	1079 (±1) / 1079(-)	—	1048	1093
Crucible for thermal analysis		W interlayer in Al_2O_3	graphite	Mo	Al_2O_3/SiO_2

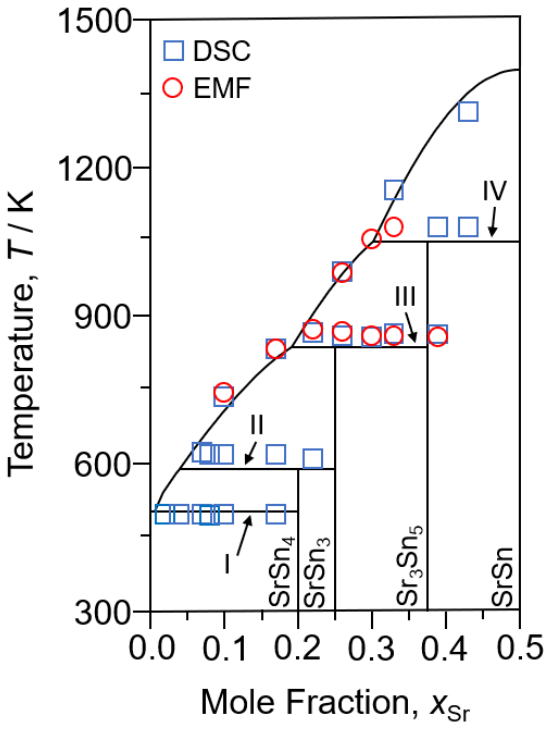

Figure 6. Transition temperatures from emf (○) and DSC (□) measurements overlaid on the partial Sr-Sn phase diagram reproduced with the ThermoCalc software using the thermodynamic parameters reported by Zhao et al.[10].

Table 4. Change in partial molar entropy, $\Delta\bar{S}_{\mathrm{Sr}}$, and partial molar entropy, $\Delta\bar{H}_{\mathrm{Sr}}$, calculated from linear fits of emf data (E_{cell} vs. T) of the Sr-Sn alloys, where $\partial E_{\mathrm{cell}}/\partial T$ and $\partial(E_{\mathrm{cell}}/T)/\partial(1/T)$ are the slopes and intercepts respectively. The standard errors in the parentheses represent the 95% confidence interval of the fit.

x_{Sr}	T / K	$\partial E_{\mathrm{cell}}/\partial T$ (μV K^{-1})	$\Delta\bar{S}_{\mathrm{Sr}}$ (J mol^{-1} K^{-1})	$\partial(E_{\mathrm{cell}}/T)/\partial(1/T)$ (mV K^{-1})	$\Delta\bar{H}_{\mathrm{Sr}}$ (kJ mol^{-1} K^{-1})	adj-R^2
0.02	909–1110	124(±3)	30	788(±3)	–152	0.954
0.04	758–1110	108(±0)	21	757(±0)	–146	0.999
0.07	758–1110	70(±0)	13	759(±0)	–146	0.993
0.08	758–1110	55(±1)	11	759(±1)	–146	0.968
0.10	755–1106	20(±1)	4	758(±1)	–146	0.879
0.17	833–1110	–11(±1)	–2	732(±1)	–141	0.566
0.22	883–1106	–40(±1)	–8	725(±1)	–140	0.937
0.26	1007–1106	–72(±6)	–14	700(±7)	–135	0.796
0.30	755–830	–207(±45)	–40	810(±37)	–170	0.832
0.30	1082–1106	–218(-)	–42	799(-)	–156	—
0.33	733–861	–138(±27)	–27	752(±21)	–154	0.867
0.33	1085–1108	–177(-)	–34	893(-)	–145	—
0.39	730–854	–246(±19)	–47	693(±15)	–172	0.971
0.43	884–1086	–143(±10)	–28	758(±10)	–134	0.964

Table 5. Non-linear fits of the temperature dependence of emf data in two-phase regions. The data were fit to $E_{\mathrm{cell}} = A + BT + CT\ln(T)$. The standard errors in the parentheses represent the 95% confidence interval of the fit.

x_{Sr}	two-phase region	T (K)	A	B ($\times 10^{-2}$)	C ($\times 10^{-3}$)	adj-R^2
0.10–0.22	L + $SrSn_3$	728–878	–1.257 (±0.634)	2.338 (±0.607)	–3.123 (±0.79)	0.979
0.26–0.39	L + Sr_3Sn_5	881–1108	–1.306 (±0.213)	1.955 (±0.171)	–2.552 (±0.217)	0.995

Table 6. Measured emf of Sr-Sn alloys (E_{cell} vs. pure Sr(s)), natural log acitivity of Sr (ln a_{Sr}), and excess partial molar Gibbs energy of Sr ($\bar{G}_{\text{Sr}}^{E}$) at 800 K, 900 K, and 1000 K.

x_{Sr}	E_{cell} (V)			ln a_{Sr}			$\bar{G}_{\text{Sr}}^{\text{E}}$ (kJ mol^{-1})		
	800 K	900 K	1000 K	800 K	900 K	1000 K	800 K	900 K	1000 K
0.02	0.887	0.899	0.911	–25.7	–23.2	–21.2	–145	–144	–143
0.04	0.844	0.855	0.865	–24.5	–22.0	–20.1	–141	–141	–140
0.07	0.815	0.822	0.829	–23.6	–21.2	–19.2	–140	–139	–138
0.08	0.803	0.809	0.814	–23.3	–20.9	–18.9	–138	–137	–136
0.10	0.774	0.776	0.778	–22.5	–20.0	–18.1	–134	–133	–131
0.17	0.744	0.722	0.721	–21.6	–18.6	–16.7	–132	–126	–124
0.22	0.744	0.689	0.685	–21.6	–17.8	–15.9	–134	–122	–120
0.26	0.744	0.668	0.619	–21.6	–17.2	–14.4	–135	–119	–108
0.30	0.714	0.668	0.619	–20.7	–17.2	–14.4	–130	–120	–109
0.33	0.688	0.668	0.619	–20.0	–17.2	–14.4	–125	–121	–110
0.39	0.696	0.668	0.619	–20.2	–17.2	–14.4	–128	–122	–112
0.43	0.578	0.564	0.550	–16.8	–14.5	–12.8	–106	–103	–99

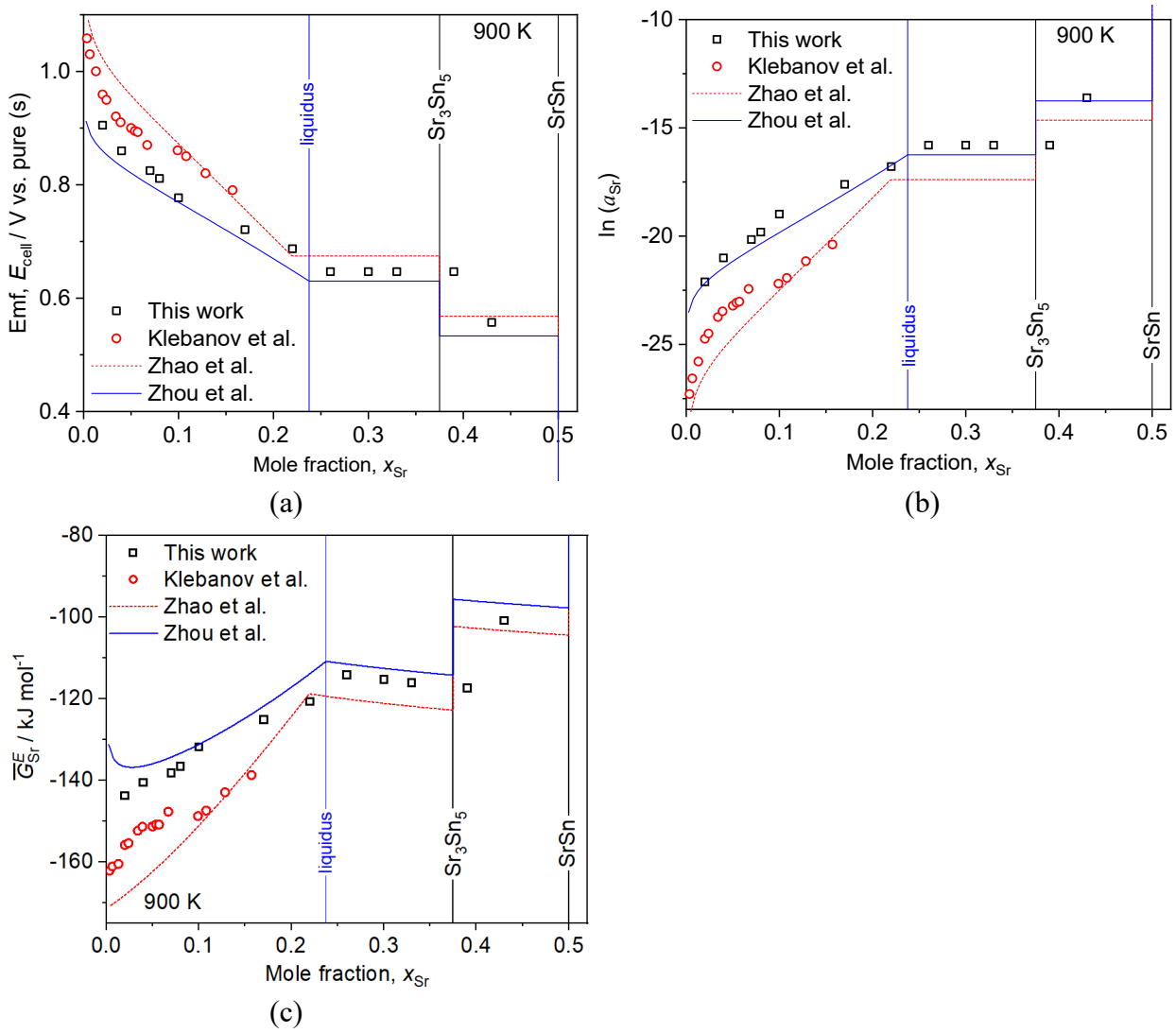

Figure 7. (a) Measured emf values, (b) natural log of activity, and (c) excess partial molar Gibbs energy as a function of x_{Sr} at 900 K, compared to the experimental results from Klebanov et al.[13] and computational results from Zhao et al.[10] and Zhou et al.[11]. The liquidus composition (x_{Sr} = 0.24) is taken from Zhou et al.